Materials Advances

ROYAL SOCIETY OF CHEMISTRY

PAPER

View Article Online
View Journal | View Issue

Cite this: *Mater. Adv.*, 2025, 6, 1710

Dynamic imidazolium phosphate@titanium dioxide ionogels as environmental pollutant removers†

Mohamed Boundor,[a] Nadia Katir *[a] and Abdelkrim El Kadib *[ab]

Received 24th October 2024,
Accepted 27th January 2025

DOI: 10.1039/d4ma01073f

rsc.li/materials-advances

Phosphate-containing ionic liquids display interesting inherent properties including versatile chemical reactivity, thermal and hydrolytic stability and biological response. This contribution focuses on synthesizing diverse imidazolium dialkylphosphates through a simple method involving *N*-quaternization of 1-alkylimidazole with trialkylphosphate. The use of these building-blocks during sol–gel polymerization of titanium alkoxide affords novel imidazolium phosphate@TiO_2 hybrid ionogels. The highest affinity of phosphate towards titanium dioxide results in covalent functionalization of the two phases through stable P–O–Ti bridges, without compromising the molecular dynamic of the embedded ionic liquids. The cationic moiety can be fully exchanged as illustrated using Na^+ and NH_4^+ providing access to iono-materials with adjustable properties. The beneficial effect of the as-prepared dynamic hybrid ionogels was clearly demonstrated by their superior efficiency in removing representative cationic dyes, pharmaceutical pollutants, and metal ions compared to unmodified, native TiO_2.

Introduction

Phosphate-containing ionic liquids stand as a new class of hydrophilic ionic liquids with notable attributes including outstanding reactivity, good thermal stability, enhanced hydrolysis resistance, and low toxicity.[1–5] They find applications in diverse fields such as biomass processing,[6–11] oil desulfurization,[12–14] medical biotechnology,[15,16] azeotropic system separation,[17–20] and organic synthesis as solvents and catalysts.[21–26] Remarkably, phosphate ionic liquids are credited for dissolving recalcitrant microcrystalline cellulose, opening exciting avenues in green and sustainable chemistry processing.[2,27–30]

Akin to conventional ionic liquids, their liquid state often impedes their use as advanced solvents and electrolytes, especially in applications requiring solid forms.[31,32] Challenges include high viscosity, low diffusion coefficients, purification and recycling difficulties, and high costs.[33]

One strategy to address these issues, particularly fluidity, is to immobilize ionic liquids on porous matrices.[34–36] This can be achieved through physical confinement inside of the porous network or covalent grafting on the surface.[34,35] The final properties can be adjusted for specific applications by modifying either the cationic or the anionic group of the starting ionic liquid as well as the selected porous carrier.[34,35,37,38] Covalent grafting requires ionic liquids bearing specific groups like trimethoxysilyl, dimethylphosphonate, or thiol, along with supports having reactive surfaces, *e.g.* hydroxyl groups in the case of silica.[34,35,39,40] For inert porous matrices like porous carbon and metal, additional surface pretreatment is required to introduce functional groups like hydroxyls.[41] Covalent attachment prevents ionic liquid migration, and mitigates drawbacks like high viscosity and slow gas diffusion while lowering costs and improving thermal and chemical stability. The fruitful combination of high surface area supports with unique ionic liquid properties lends utility to various domains including catalysis, gas separation, energy storage, lubrication enhancement, and carbon material production.[34,35,37,39,40]

While the interaction of ionic liquids and silica hosts has been deeply studied, including either the entrapped or covalently linked forms,[42–50] this was not the case for non-siliceous metal oxide carriers, where few examples were comparatively reported.[51–53] With this aim, we herein report a straightforward synthesis of phosphate-containing ionic liquids (**PIL$_n$**) featuring 1,3-dialkylimidazolium paired with various dialkylphosphates. These ionic building blocks were used to develop novel nanostructured hybrid ionogels (**PIL$_n$@TiO$_2$**) through sol–gel processing, involving the co-condensation of the phosphate anion with TiO_2. Owing to the highest affinity of phosphate to titanium

[a] *Euromed University of Fes, UEMF, Morocco. E-mail: n.katir@ueuromed.org*
[b] *Hassan II Academy of Science and Technology, Rabat, Morocco. E-mail: a.elkadib@ueuromed.org*

† Electronic supplementary information (ESI) available: Apparatus and analytical procedures; experimental details; infrared spectra; supplementary liquid and solid NMR spectra; N_2 adsorption/desorption isotherms and textural parameters; supplementary XRD and Raman spectra. See DOI: **https://doi.org/10.1039/d4ma01073f**

dioxide, the embedded ionic liquids form stable Ti–O–P bonds with the ceramic phase. The dynamic character of these hybrid ionogels was substantiated through spectroscopic analysis and further corroborated through cationic exchange. The imidazolium cation was indeed replaced by Na^+ and NH_4^+ cations, without disrupting the way that anionic phosphate binds to titanium dioxide. We further demonstrate the efficiency of **PIL$_n$@TiO$_2$** for the removal of methylene blue as a representative cationic dye, tetracycline as a representative pharmaceutical antibiotic, and $Fe^{(III)}$ and $Au^{(III)}$ as metal ions from aqueous solutions.

Results and discussion

Synthesis of phosphate ionic liquids (PIL$_n$)

Phosphate ionic liquids were prepared *via* direct alkylation, involving the *N*-quaternization of 1-alkylimidazole with a slight excess of trialkylphosphate (1.2 eq.) under a nitrogen atmosphere (Scheme 1a). ^{1}H NMR monitoring showed that the quaternization kinetics slowed as the phosphate's alkyl chain length increased. In a 1 : 1.2 ratio of alkylimidazole to trialkylphosphate, complete conversion was achieved after two days at 80 °C with trimethylphosphate *versus* three days at 120 °C with tributylphosphate. All ionic liquids were isolated in a quantitative yield of ~99% and are liquid at room temperature.

The FTIR spectra of the synthesized phosphate ionic liquids show bands between 2800 and 3000 cm^{-1} corresponding to the stretching vibrations of alkyl groups (–CH_2– and –CH_3), and bands between 3100 and 3200 cm^{-1} for the imidazolium ring (–C–H). C=C vibrations appear at 1575 cm^{-1}, while the P=O vibration is observed between 1177 and 1239 cm^{-1}.[54] Additionally, a band at ~3400 cm^{-1} indicates the presence of absorbed water, showing that the hydrophilicity of phosphate ionic liquids decreases with increasing carbon chain length (Fig. S1, ESI†).

Multinuclear NMR spectroscopy confirmed the structure of the synthesized phosphate ionic liquids. The ^{31}P NMR spectrum of **PIL$_1$** reveals a complete disappearance of the signal of the starting trimethylphosphate at 3.8 ppm and the appearance in turn of a new septuplet signal at 2.87 ppm (Fig. 1a), due to the coupling of phosphorus with six equivalent protons from the methoxy groups, with a coupling constant of $^3J_{P-H}$ = 10.7 MHz.[54] This multiplicity indicates that each phosphate anion is counterbalanced by one imidazolium cation, which consequently excludes the formation of ionic liquids in dimeric

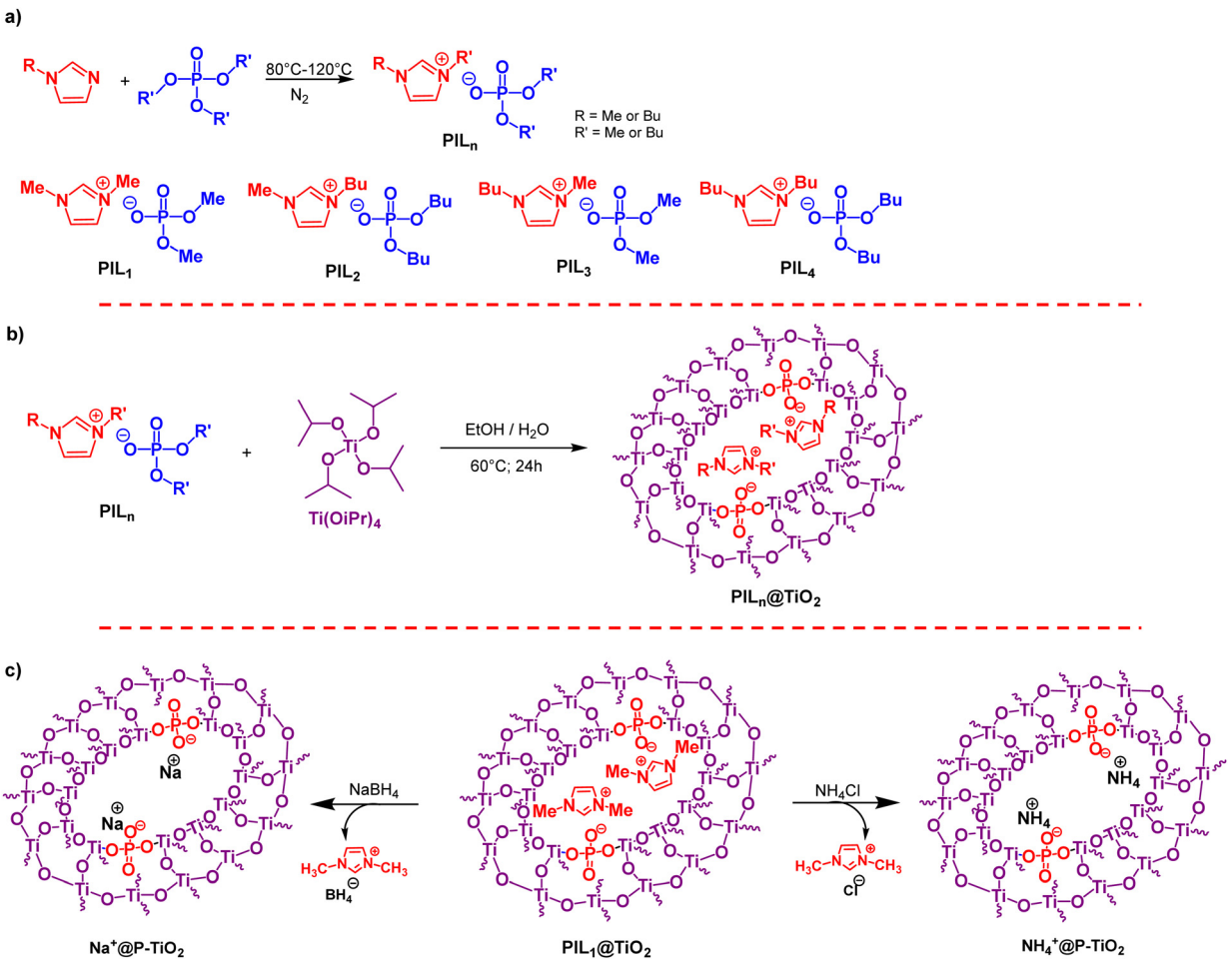

Scheme 1 (a) Synthesis of the PILn used in this study, (b) sol–gel method for preparing **PIL$_n$@TiO$_2$** ionogels and (c) cation exchange carried out on **PIL$_n$@TiO$_2$**.

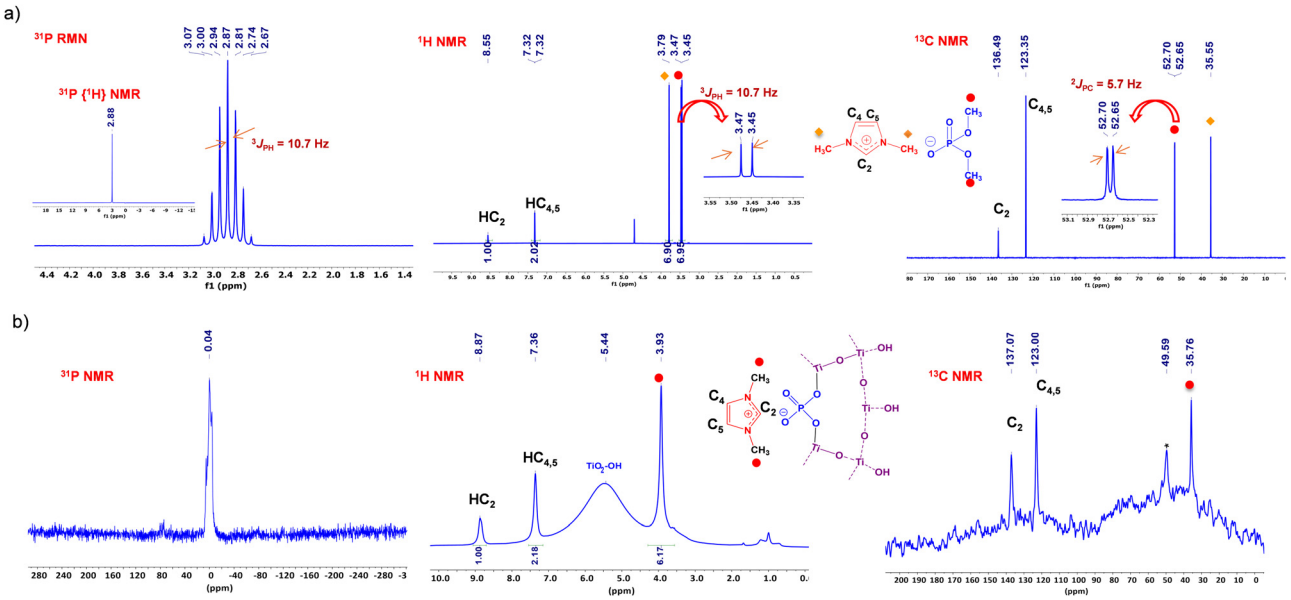

Fig. 1 (a) Liquid-state (^{31}P, ^{1}H and ^{13}C) NMR of PIL_1 and (b) solid-state (^{31}P, ^{1}H and ^{13}C) MAS NMR of **PIL_1@TiO_2**.

or trimeric states during alkylation. In the ^{1}H NMR spectrum of **PIL_1**, the imidazolium proton appears at 8.55 ppm, with symmetric protons at positions 4 and 5 showing a doublet at 7.32 ppm. A doublet at 3.97 ppm corresponds to the six symmetric hydrogens on the two methyl groups at positions 1 and 3, with a weak coupling constant of 0.7 Hz. The dimethylphosphate anion signal was shown at 3.46 ppm, with a coupling constant of $^{3}J_{P-H}$ = 10.7 Hz that is fully consistent with the ^{31}P NMR spectrum as discussed above. The ^{13}C NMR spectrum of **PIL_1** displays peaks at 136.49, 123.35, and 35.55 ppm, corresponding to the carbons C2, C3, and N–CH_3, respectively. The signal from the dimethylphosphate carbon appears as a doublet at 52.67 ppm, indicating a coupling constant of $^{2}J_{C-P}$ = 5.7 Hz between carbon and phosphorus (Fig. 1a). The chemical structure of the other phosphate ionic liquids was also elucidated by multinuclear (^{1}H, ^{13}C, ^{31}P) NMR spectroscopy and provided in the experimental section (Fig. S2–S4, ESI†).

Preparation of PLI_n@TiO_2 hybrid ionogels

The synthesis of **PIL_n@TiO_2** was achieved through a two-step process involving hydrolysis and condensation of titanium tetraisopropoxide ($Ti(OiPr)_4$) in the presence of **PIL_n** (Scheme 1b). Initially, phosphate-containing ionic liquid was dissolved in ethanol, and then $Ti(OiPr)_4$ was added at a 1 : 20 molar ratio. After stirring for 15 minutes, water (2/5 the volume of ethanol) was introduced, resulting in a cloudy solution because of the extent of titanium alkoxide hydrolysis and condensation. The gel was subsequently heated at 60 °C for 24 hours. The resulting solid was filtered, washed with ethanol, and dried at 60 °C to yield a white solid powder of **PIL_n@TiO_2** ionogel.

The structural composition of the resulting materials has been elucidated through infrared spectroscopy (FTIR) and multinuclear solid-state MAS NMR spectroscopy, including ^{31}P, ^{1}H and ^{13}C nuclei. The FTIR spectrum of **PIL_1@TiO_2** reveals key bands, including Ti–O–Ti bending vibration at 445 cm^{-1}, hydroxyl groups at 3600–2700 cm^{-1}, and OH groups of physiosorbed water at 1638 cm^{-1}. C=C vibration of the imidazolium cation appears at 1575 cm^{-1}, while the P=O frequency of the phosphate group resonates at 1170 cm^{-1}. The broader band at 1105 cm^{-1} is assignable to P–O–Ti stretching vibration, thereby confirming the covalent anchoring of the phosphate anion to the TiO_2 surface.[55] Materials with long alkyl chains show weak C–H stretching modes at 2853–2919 cm^{-1}, indicating the retention of **PIL**'s organic motifs within the TiO_2 framework (Fig. S5, ESI†).

The solid-state ^{31}P MAS NMR spectrum of various **PIL_n@TiO_2** exhibits a well resolved single signal ranging from approximately −0.04 to −1.32 ppm, attributed to the mineral phase bridged by a phosphate anion through the Ti–O–P(O)–O linker (Fig. 1b and Fig. S6, ESI†). This notable shift toward negative values, from 2.87 ppm for **PIL_1** to −0.04 ppm for **PIL_1@TiO_2**, can be attributed to the formation of at least one Ti–O–P bond.[56] The variation in phosphorus chemical shifts observed with different **PIL_n** is associated with the nature of the counter-cation. When the positive charge of the cation decreases due to its inductive donor groups (such as butyl), the negative charge of its phosphate counter-anion becomes more significant, leading to enhanced shielding of the phosphorus. This suggests that the sol–gel process induces condensation between the titanium alkoxide and the alkoxy groups of the phosphate component of the ionic liquid, while maintaining the anionic character stabilized by its counter-cation. The cation remains intact, as confirmed by ^{1}H and ^{13}C NMR spectroscopy.

Surprisingly, the solid-state ^{1}H MAS NMR spectrum of **PIL_1@TiO_2** reveals intense and well-defined peaks corresponding to the protons of the 1,3-dimethylimidazolium cation, alongside a broad peak at 5.44 ppm attributed to the Ti–OH hydroxyl protons on the TiO_2 surface (Fig. 1b). The signal at

8.86 ppm corresponds to the proton in position 2 of the imidazole ring, and the peak at 7.35 ppm represents the two hydrogens in positions 4 and 5 due to molecular symmetry. Additionally, the protons of the methyl group attached to nitrogen appear at 3.92 ppm. The integral intensities correlate perfectly with the number of protons present in the cationic part of the **PIL$_1$**. Therefore, the absence of the methoxy group peak of the phosphate anion indicates their hydrolysis and release during the sol–gel process. ^{1}H MAS NMR spectra of **PIL$_2$@TiO$_2$** and **PIL$_3$@TiO$_2$** show identical peaks corresponding to 1-butyl-3-methylimidazolium with their integration indicating that they exclusively correspond to the protons of the cation (Fig. 1b and Fig. S7, ESI†). This further confirms the removal of butoxy groups from the anion during the sol–gel process. This phenomenon also occurs in **PIL$_4$@TiO$_2$**, where all the peaks correspond exclusively to the carbon proton of the butylic groups attached to the nitrogen in the ring (Fig. S7, ESI†). The noticeably narrow signals observed for these ionogels reflect a pronounced dynamicity of the solid framework and suggest that the ionic character of the network remains dominant in the solid state, despite the significant network reticulation occurring during sol–gel polymerization.[42]

The solid-state ^{13}C MAS NMR of **PIL$_1$@TiO$_2$** exhibits characteristic signals of the 1,3-dimethylimidazolium cation, with carbon resonances of N–CH–N, N–CH═CH–N, and N–CH$_3$ observed at approximately 137, 122, and 35 ppm, respectively (Fig. 1b). The carbon peak from the anionic part of the starting methyl phosphate, expected around 53 ppm, vanishes. Similarly, in the case of ionogels with other **PIL$_n$**, the presence of cationic components was also noticed (Fig. S8, ESI†). These spectra collectively demonstrate the absence of peaks corresponding to carbons from the anionic part, consolidating its consumption and the creation of new P–O–Ti bonds during mineralization, while preserving the structure of the cation and its ionic interaction with the phosphate anion.

Thermogravimetric analysis was conducted to assess the thermal stability of these hybrid ionogels. Nearly the same weight degradation of 4% could be observed until 200 °C for all **PIL$_n$@TiO$_2$** due to the evaporation of water, alcohols, and physically adsorbed species. Subsequently, a much steeper slope takes place above 230 °C due to the decomposition of 1,3-dialkylimidazolium, with mass loss increasing with the cation's size (Fig. S9, ESI†). Therefore, ionogels with the same cation exhibit similar thermal behavior. Moreover, compared to TiO$_2$ prepared under similar conditions, the weight loss beyond 230 °C in **PIL$_1$@TiO$_2$** matches the calculated mass of the 1,3-dimethylimidazolium cation, suggesting its complete incorporation inside of the network (Fig. S9, ESI†).

X-ray diffraction (XRD) analysis of **PIL$_n$@TiO$_2$** shows exclusively crystalline peaks of the anatase phase at 25.2, 37.8, 47.8, 53.9, 62.5, 69.2 and 74.8 corresponding respectively to the (101), (004), (200), (105), (213), (116) and (215) planes (Fig. 2a). The average crystallite size estimated from Scherrer's formula is 5 nm. However, the absence of polyphosphate or layered titanate phosphate peaks indicates that phosphorus is well dispersed in the composite and that TiO$_2$ is sufficiently doped with phosphorus.[57–60] Additionally, another peak was observed at 18° for the **PIL$_4$@TiO$_2$** ionogel, which could be attributed to the packing of imidazolium ring moieties. This peak may indeed result from the large size of the cation, whose long alkyl chains could facilitate the formation of a certain organic periodicity, reminiscent of the one seen in metal–organic frameworks. For the smaller ionic liquid, this peak was observed at 17.9° when the **PIL$_1$** content was increased in the **PIL$_1$@TiO$_2$** to a molar ratio of 1 : 5 (LIP$_1$: Ti(OiPr)$_4$) (Fig. S10, ESI†). Raman spectroscopy confirms the formation of anatase phase in **PIL$_n$@TiO$_2$**, with distinct vibrational modes observed at 144, 396, 509, and 634 cm^{-1} corresponding to E$_g$, B$_{1g}$ (O–Ti–O bending), A$_{1g}$ (Ti–O stretching), and E$_g$ (Ti–O stretching), respectively (Fig. 2b).[61]

Nitrogen adsorption–desorption of **PIL$_n$@TiO$_2$** shows an isotherm profile of type IV, with a hysteresis loop typical of mesoporous materials (Fig. S11, ESI†). While a surfactant-free design was chosen here for its simplicity and cost-effectiveness, **PIL$_n$@TiO$_2$** displayed a consistent specific surface area of 200 m^2 g^{-1}. The specific surface area is slightly higher for hybrid ionogels with asymmetric cationic and larger **PILs** (Table S1, ESI†).

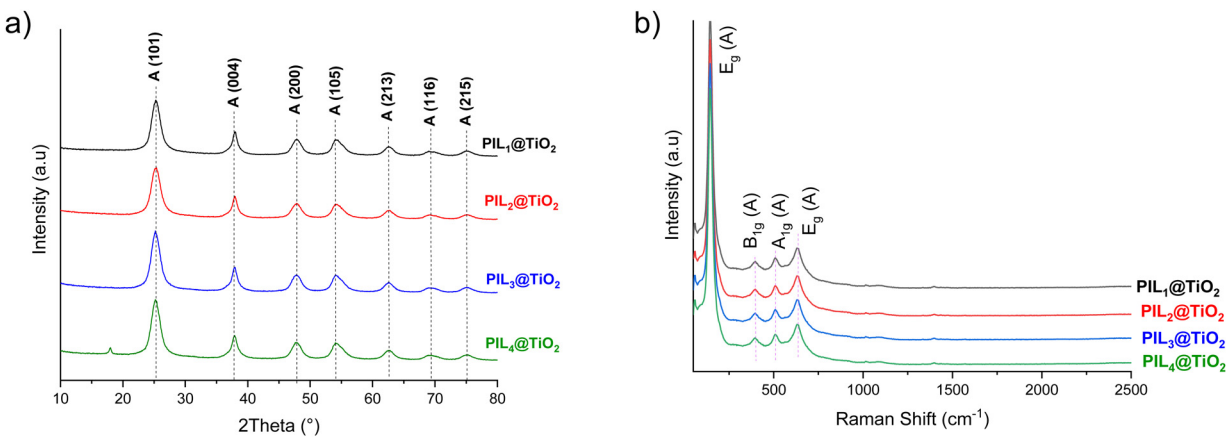

Fig. 2 (a) XRD patterns and (b) Raman spectra of **PIL$_n$@TiO$_2$**.

Therefore, both the size and volume of the pores increase with the size of the anion, suggesting that the inorganic burst initially nucleates and then condenses with the anionic phosphate near to the surface. It is reasonable to assume the critical role of **PIL$_n$** serving as a structure-directing agent and confining medium to grow and crystallize discrete mesoporous anatase nanoparticles.[62,63]

X-ray photoelectron spectroscopy (XPS) analysis of **PIL$_1$@TiO$_2$** reveals the presence of Ti, O, P, N, and C, consistent with the expected chemical composition of the final ionogel (Fig. 3a). The C 1s spectrum can be deconvoluted into three different species, namely C–H, CH_3–N and carbons from the imidazolium ring N–C═C–N and N═C–N components, with binding energies centered at 284.8, 286.3, and 288.6 eV, respectively.[64] In the nitrogen region, the peak at 401.3 eV corresponds to the nitrogen (N^+) in the imidazolium cation, while the smaller peak at 398.7 eV is attributed to the non-ionized nitrogen in the ring.[65] These results indicate that the imidazolium cation retains its structural integrity and remains cationic. For oxygen species, the O 1s spectrum displays signals at 529.8 eV and 533.0 eV for oxygen in the oxide lattice (Ti–O–Ti) and on the surface (Ti–═OH), respectively.[66] The peak at 531.5 eV is associated with P–O–Ti and P═O.[67] In the phosphorus region, the P 2p peak can be deconvoluted into two main components located at 133.3 and 134.1 eV assigned to the Ti–O–P bond and phosphate species, respectively.[68,69] The absence of a peak at 133.1 eV corresponding to the P–O–C bond indicates that the two methoxyl groups of **PIL$_1$** have been hydrolyzed and condensed with the TiO_2 network.[69] The high-resolution Ti 2p spectrum was deconvoluted into peaks at 458.5 eV (Ti $2p_{3/2}$) and 462.2 eV (Ti $2p_{1/2}$), confirming Ti–O bonds in the Ti^{4+} state. The negative shift of Ti $2p_{3/2}$ from the typical 459.3 eV in TiO_2 is attributed to phosphorus doping and oxygen defects.[70]

Scanning electron microscopy (SEM) images of **PIL$_1$@TiO$_2$** reveal the formation of aggregates of spherical nanoparticles approximately 100 nm in size (Fig. 3b). The uniform size of the primary particles and the absence of large crystals indicate a controlled sol–gel polymerization, corroborating our assumptions that **PIL$_1$** plays a pivotal role in directing the nucleation and growth of the anatase mineral phase. Energy-dispersive X-ray spectroscopy (EDX) mapping of the elemental composition of both organic and inorganic phases reveals a uniform distribution of phosphorus and titanium throughout the microstructure. This provides convincing evidence for the intimate hybridization of **PIL$_1$** and **TiO$_2$** within the network, without phase separation or segregation (Fig. 3b).

Cation exchange on PIL$_1$@TiO$_2$

PIL$_1$@TiO$_2$ was next subjected to cation exchange. This route could provide a route for expanding the molecular diversity of the dynamic ionogels and further tailoring its properties. The exchange was executed using two reagents ($NaBH_4$ and NH_4Cl) to replace 1,3-dimethylimidazolium cations in **PIL$_1$@TiO$_2$** with Na^+ and NH_4^+, resulting, respectively, in the formation of **Na^+@P-TiO$_2$** and **NH_4^+@P-TiO$_2$** (Scheme 1c).

The exchange reaction was performed in ethanol, where **PIL$_1$@TiO$_2$** was dispersed. A stoichiometric amount of the exchanging agent relative to 1,3-dimethylimidazolium was added. After stirring for 4 hours, the mixture was filtered and thoroughly washed with ethanol, and the solid was dried at 60 °C. Cation exchange was monitored by FTIR analysis, focusing on the C═C band of the imidazolium ring at approximately 1573 cm^{-1}. The absence of this signature for **NH_4^+@P-TiO$_2$** indicates complete exchange of the 1,3-dimethylimidazolium. In contrast, for **Na^+@P-TiO$_2$**, the sharp band transformed into a broad band (Fig. S12, ESI†). Solid-state ^{31}P MAS NMR spectroscopy of **Na^+@P-TiO$_2$** and **NH_4^+@P-TiO$_2$** showed broad signals at δ = −0.17 ppm and δ = −1.07 ppm (Fig. S13, ESI†). These peaks indicate the intactness of the phosphate moiety after the exchange reaction, with the slight chemical shift difference attributed to the nature of the counter-cation. Solid-state ^{13}C MAS NMR confirms the disappearance of the characteristic peaks of the 1,3-dimethylimidazolium cation (Fig. S14, ESI†), demonstrating effective exchange with both sodium Na^+ and ammonium NH_4^+ cations.

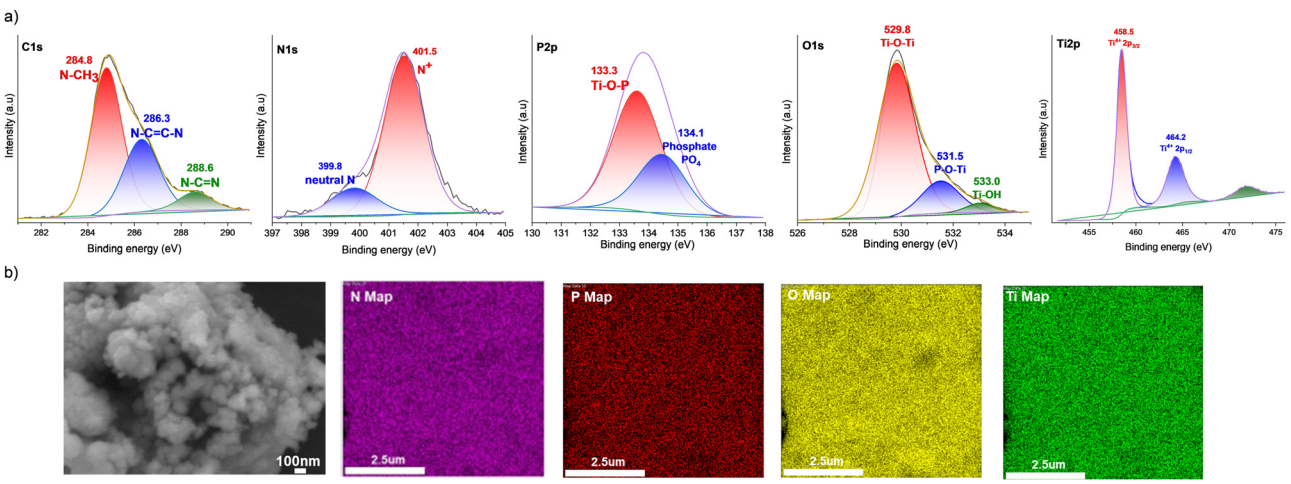

Fig. 3 (a) XPS spectra and (b) SEM image/elemental analysis mapping by SEM-EDX of N, P, O and Ti of **PIL$_1$@TiO$_2$**.

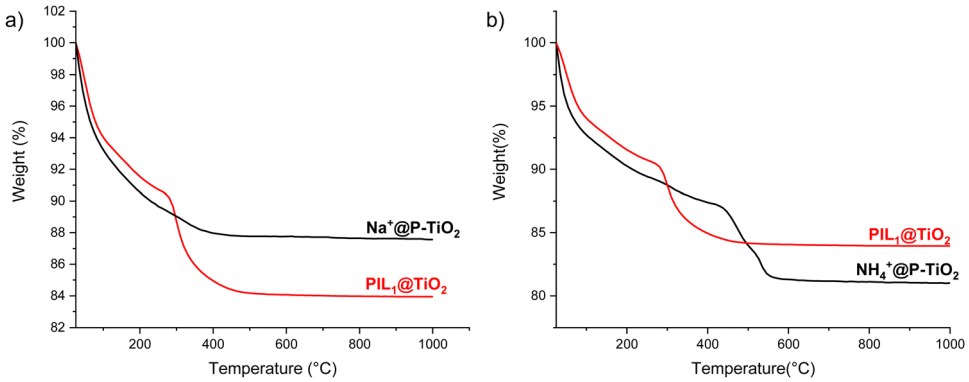

Fig. 4 TGA analysis of (a) Na^+@P-TiO_2 and (b) NH_4^+@P-TiO_2 compared with the starting material **PIL$_n$@TiO$_2$**.

The thermal weight degradation profile of **Na^+@P-TiO_2** was compared to that of **PIL$_1$@TiO$_2$** (Fig. 4). The significant mass loss observed in the original ionogel above 230 °C was absent in the inorganic material, with the mass difference between the two materials from 500 °C onward corresponding to the 4% mass of the 1,3-dimethylimidazolium cation present before the exchange. Similarly, cation exchange with NH_4Cl shifted the degradation onset from 260 °C in **PIL$_1$@TiO$_2$** to 410 °C in **NH_4^+@P-TiO_2**, demonstrating enhanced thermal stability of the exchanged materials compared to the original ionogels.

Nitrogen adsorption–desorption isotherms of both materials show a hysteresis loop characteristic of open mesoporous structures (Fig. S15, ESI†). **Na^+@P-TiO_2** displays a specific surface area of 194 $m^2\ g^{-1}$ and an average pore size of 5 nm, indicating a slight shrinkage of the network during exchange. **NH_4^+@P-TiO_2** exhibits a specific surface area of 254 $m^2\ g^{-1}$, which is 56 $m^2\ g^{-1}$ greater than that of the parent ionogel. After cation exchange, both materials retain the crystalline anatase phase, as confirmed by XRD spectra with well-resolved peaks and an average crystallite size of about 5 nm (Fig. S16, ESI†). Raman spectroscopy further supports these findings by revealing the characteristic anatase modes consistent with the XRD data (Fig. S17, ESI†).

Removal of organic pollutants and metal ions from water

Ionic liquids display great affinity for chemical and metal pollutants, but are difficult to recover from the medium because of their inherent solubility.[71] To address this issue, supported ionic liquids including ionogels present a scalable alternative. **PIL$_n$@TiO$_2$** materials were consequently tested for the removal of cationic methylene blue (MB) dye and tetracycline antibiotic (TC), and two metal ions namely $Fe^{(III)}$ and $Au^{(III)}$ from aqueous solutions.

Fig. 5 and Fig. S18, and S19 (ESI†) illustrate the removal efficiency (%) and adsorption capacity (mg g^{-1}) of MB, TC,

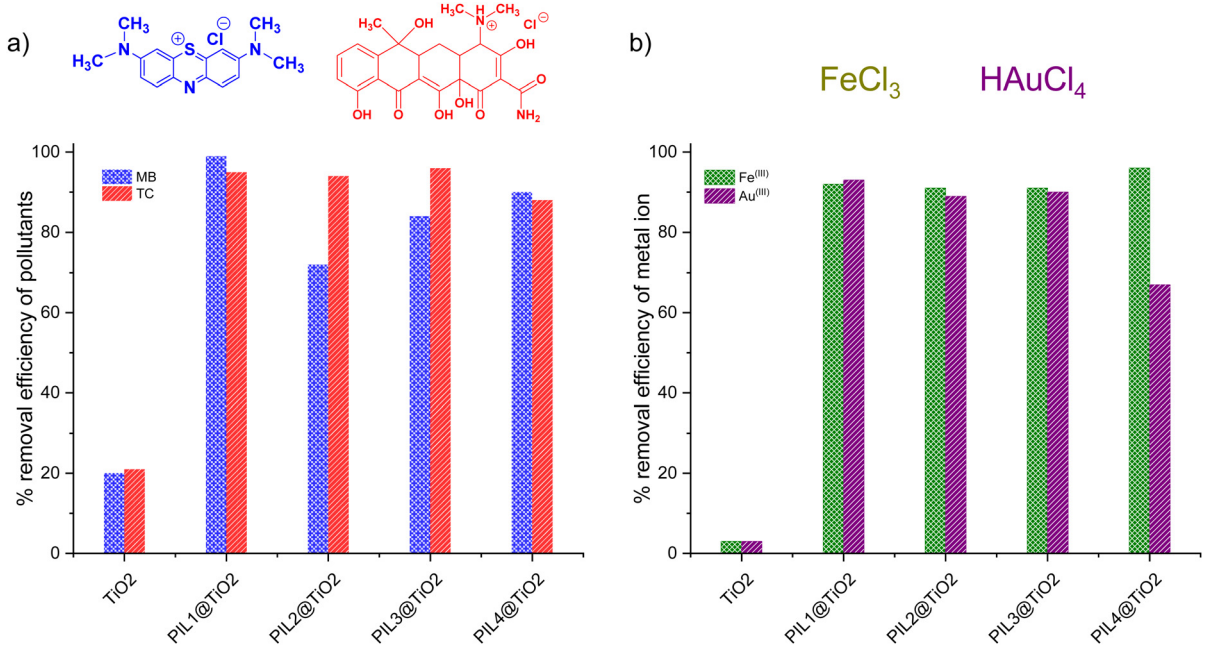

Fig. 5 Removal of (a) methylene blue (MB) and tetracycline (TC), and (b) removal of $Fe^{(III)}$ and $Au^{(III)}$ using TiO_2 and **PIL$_n$@TiO2** materials.

$Fe^{(III)}$ and $Au^{(III)}$ using both unmodified TiO_2 and **PIL$_n$@TiO$_2$**. Pristine TiO_2 enables only 20% removal of methylene blue, with a low adsorption capacity of 6×10^{-2} mg g^{-1}, contrasting with the enhanced performance reached using **PIL$_n$@TiO$_2$** (Fig. 5a and Fig. S20, ESI†). The highest removal efficiency (99%) was recorded for **PIL$_1$@TiO$_2$** (99%) and an adsorption capacity of 32×10^{-2} mg g^{-1}.

A similar trend was also observed for the uptake of tetracycline, with unmodified TiO_2 being able to remove only 21%, with an adsorption capacity of 9.33 mg g^{-1}. Comparatively, the removal efficiency attained by **PIL$_n$@TiO$_2$** exceeds 88%, with adsorption capacities greater than 39 mg g^{-1}. **PIL$_3$@TiO$_2$** stands as the most effective, with a removal efficiency of 96% and an adsorption capacity of 42.61 mg g^{-1}.

Ionogels also offer substantial potential for metal extraction due to the immobilization of active chemical groups, which leads to a marked increase in the binding capacity of materials for a wide range of metal ions.[72] In our study, unmodified TiO_2 demonstrated marginal uptake of 3% for $Fe^{(III)}$ removal, with an adsorption capacity of 0.15 mg g^{-1}. In contrast, regardless of their composition, **PIL$_n$@TiO$_2$** displayed nearly quantitative removal efficiency that exceeds 91%, with **PIL$_4$@TiO$_2$** being the best scavenger (96% removal and an adsorption capacity of 4.77 mg g^{-1}). Unmodified TiO_2 was also ineffective for $Au^{(III)}$ uptake, enabling only 3% removal and an adsorption capacity of 0.85 mg g^{-1}. **PIL$_n$@TiO$_2$** showed spectacular improvements, with **PIL$_1$@TiO$_2$** achieving the highest removal efficiency (93%) and an adsorption capacity of 25.9 mg g^{-1}. Notably, during the adsorption process, $Au^{(III)}$ was spontaneously reduced to $Au^{(0)}$ nanoparticles, as evidenced by the color variation of **PIL$_n$@TiO$_2$** powders from white to dark purple,[73–75] after filtration and drying of the adsorbents (Fig. S21, ESI†). Overall, these results highlight the interesting performance of **PIL$_n$@TiO$_2$** compared to unmodified TiO_2, with the resulting ionogels being competitive compared to standard absorbents (Table S2, ESI†). Besides, the reducing ability of these ionogels as evidenced for gold, and their high-surface area open new channels of possibilities in the field of heterogeneous (photo)catalysis.

Conclusions

In summary, this study focused on the straightforward preparation of a set of dialkylphosphate-containing ionic liquids, using a catalyst-free, solvent-free, single-step synthesis. Next, the co-condensation of these ionic building-blocks with titanium alkoxide resulted in the formation of novel titanium oxide entrapping imidazolium phosphate ionic liquids. These dynamic hybrid ionogels exhibit several distinctive features, including the formation of stable P–O–Ti covalent bonds, while retaining the ionic character and the mobility of organic moieties as shown by solid-state ^{1}H and ^{13}C NMR of the imidazolium cation, an open porous network formed under surfactant-free conditions, and a crystalline framework built from discrete anatase nanoparticles. The potential for cation exchange within the iono-materials was demonstrated, affecting thermal and structural properties. Additionally, the hybrid ionogels showed a remarkable ability to remove chemical pollutants and metal ions from water, showcasing their environmental relevance.

Author contributions

The manuscript was written through contributions of all authors. All authors have given approval to the final version of the manuscript.

Conflicts of interest

There are no conflicts to declare.

Acknowledgements

This work was financially supported by UEMF.

References

1 E. Kuhlmann, S. Himmler, H. Giebelhaus and P. Wasserscheid, *Green Chem.*, 2007, **9**, 233–242.
2 T. Endo, S. Yoshida and Y. Kimura, *Cryst. Growth Des.*, 2020, **20**, 6267–6271.
3 P. D. Vu, A. J. Boydston and C. W. Bielawski, *Green Chem.*, 2007, **9**, 1158–1159.
4 M. Musiał, E. Zorebski, K. Malarz, M. Kuczak, A. Mrozek-Wilczkiewicz, J. Jacquemin and M. Dzida, *ACS Sustainable Chem. Eng.*, 2021, **9**, 7649–7657.
5 K. D. Weaver, H. J. Kim, J. Sun, D. R. MacFarlane and G. D. Elliott, *Green Chem.*, 2010, **12**, 507–513.
6 W.-T. Wang, J. Zhu, X.-L. Wang, Y. Huang and Y.-Z. Wang, *J. Macromol. Sci. Chem., Part B*, 2010, **49**, 528–541.
7 M. Feng, X. Lu, L. Wang, J. Zhang, S. Yang, C. Shi, Q. Zhou and S. Zhang, *ACS Sustainable Chem. Eng.*, 2019, **7**, 11990–11998.
8 L. Wang, Y. Nie, X. Zhang, S. Zeng, S. Zhang and S. Zheng, *Chem. Eng. Technol.*, 2016, **39**, 979–986.
9 J.-i Horinaka, A. Okamoto and T. Takigawa, *Int. J. Biol. Macromol.*, 2016, **91**, 789–793.
10 M. A. Martins, U. Domanska, B. Schröder, J. A. Coutinho and S. P. Pinho, *ACS Sustainable Chem. Eng.*, 2016, **4**, 548–556.
11 C. Kornpointner, A. S. Martinez, M. Schnürch, H. Halbwirth and K. Bica-Schröder, *Green Chem.*, 2021, **23**, 10079–10089.
12 K. Desai, S. Dharaskar, J. Pandya, S. Shinde and V. Vakharia, *Process Saf. Environ. Prot.*, 2022, **166**, 512–523.
13 H. Gao, S. Zeng, X. Liu, Y. Nie, X. Zhang and S. Zhang, *RSC Adv.*, 2015, **5**, 30234–30238.
14 Y. Chen, F. Mutelet and J.-N. Jaubert, *J. Chem. Eng. Data*, 2014, **59**, 603–612.
15 M. Smiglak, J. M. Pringle, X. Lu, L. Han, S. Zhang, H. Gao, D. R. Macfarlane and R. D. Rogers, *Chem. Commun.*, 2014, **50**, 9228–9250.

16 M. Moniruzzaman, N. Kamiya and M. Goto, *J. Colloid Interface Sci.*, 2010, **352**, 136–142.
17 X. Han, Y. Wang and Q. Li, *J. Chem. Eng. Data*, 2022, **67**, 2418–2425.
18 Z. Zhang, X. Zhao, Y. Wang, Y. Ma and G. Li, *Sep. Purif. Technol.*, 2022, **287**, 120491.
19 K. Yue and G. Zhou, *J. Mol. Liq.*, 2022, **348**, 118404.
20 F. Chen, L. Zhang, Z. Liu and G. Yu, *Ind. Eng. Chem. Res.*, 2020, **59**, 13271–13282.
21 A. Zicmanis and L. Anteina, *Tetrahedron Lett.*, 2014, **55**, 2027–2028.
22 Z. I. Ishak, N. A. Sairi, Y. Alias, M. K. T. Aroua and R. Yusoff, *Chem. Eng. J.*, 2016, **297**, 128–138.
23 T. Ståhlberg, M. G. Sørensen and A. Riisager, *Green Chem.*, 2010, **12**, 321–325.
24 S. Zhang, L. Dias Goncalves, H. Lefebvre, M. Tessier, B. Rousseau and A. Fradet, *ACS Macro Lett.*, 2012, **1**, 1079–1082.
25 M. A. Redouane, N. Khiri-Meribout, S. Benzerka and A. Debache, *Heterocycl. Commun.*, 2019, **25**, 167–179.
26 M. Y. Machado and R. Dorta, *Synthesis*, 2005, 2473–2475.
27 J. Vitz, T. Erdmenger, C. Haensch and U. S. Schubert, *Green Chem.*, 2009, **11**, 417–424.
28 M. T. Clough, J. A. Griffith, O. Kuzmina and T. Welton, *Green Chem.*, 2016, **18**, 3758–3766.
29 S. Bahrani, S. Raeissi and M. Sarshar, *Bioresour. Technol.*, 2015, **185**, 411–415.
30 D. Silva and E. Bogel-Łukasik, *Green Chem.*, 2017, **19**, 4048–4060.
31 A. K. Tripathi, *Mater. Today Energy*, 2021, **20**, 100643.
32 H. Hu, J. Li and X. Ji, *Chem. – Eur. J.*, 2024, **30**, e202302826.
33 N. Gao, Y. Yang, Z. Wang, X. Guo, S. Jiang, J. Li, Y. Hu, Z. Liu and C. Xu, *Chem. Rev.*, 2023, **124**, 27–123.
34 S. Zhang, J. Zhang, Y. Zhang and Y. Deng, *Chem. Rev.*, 2017, **117**, 6755–6833.
35 M. Dong, K. Zhang, X. Wan, S. Wang, S. Fan, Z. Ye, Y. Wang, Y. Yan and X. Peng, *Small*, 2022, **18**, 2108026.
36 M.-A. Néouze, J. Le Bideau, P. Gaveau, S. Bellayer and A. Vioux, *Chem. Mater.*, 2006, **18**, 3931–3936.
37 E. H. Lahrar, A. Belhboub, P. Simon and C. Merlet, *ACS Appl. Mater. Interfaces*, 2019, **12**, 1789–1798.
38 Y. Chen, Z. Chang, Y. Liu, X. Wan, T. Wang, Z. Zhou and G. Li, *Eur. Polym. J.*, 2024, **210**, 112992.
39 B. Xin and J. Hao, *Chem. Soc. Rev.*, 2014, **43**, 7171–7187.
40 Q. Dou, L. Liu, B. Yang, J. Lang and X. Yan, *Nat. Commun.*, 2017, **8**, 2188.
41 M. J. Park, J. K. Lee, B. S. Lee, Y.-W. Lee, I. S. Choi and S.-G. Lee, *Chem. Mater.*, 2006, **18**, 1546–1551.
42 R. Göbel, P. Hesemann, J. Weber, E. Möller, A. Friedrich, S. Beuermann and A. Taubert, *Phys. Chem. Chem. Phys.*, 2009, **11**, 3653–3662.
43 B. Gadenne, P. Hesemann and J. J. Moreau, *Chem. Commun.*, 2004, 1768–1769.
44 N. Abdou, B. Alonso, N. Brun, P. Landois, A. Taubert, P. Hesemann and A. Mehdi, *Mater. Chem. Front.*, 2022, **6**, 939–947.
45 N. Abdou, B. Alonso, N. Brun, S. Devautour-Vinot, M. Paillet, P. Landois, A. Mehdi and P. Hesemann, *J. Phys. Chem. C*, 2022, **126**, 20937–20945.
46 N. Abdou, P. Dieudonné-George, N. Brun, A. Mehdi and P. Hesemann, *Phys. Chem. Chem. Phys.*, 2022, **24**, 21853–21862.
47 J. Le Bideau, L. Viau and A. Vioux, *Chem. Soc. Rev.*, 2011, **40**, 907–925.
48 J. Le Bideau, P. Gaveau, S. Bellayer, M.-A. Neouze and A. Vioux, *Phys. Chem. Chem. Phys.*, 2007, **9**, 5419–5422.
49 K. Lunstroot, K. Driesen, P. Nockemann, C. Görller-Walrand, K. Binnemans, S. Bellayer, J. Le Bideau and A. Vioux, *Chem. Mater.*, 2006, **18**, 5711–5715.
50 A. El Kadib, P. Hesemann, K. Molvinger, J. Brandner, C. Biolley, P. Gaveau, J. J. Moreau and D. Brunel, *J. Am. Chem. Soc.*, 2009, **131**, 2882–2892.
51 A. Dutta, D. K. Mishra, D. Kundu, U. Mahanta, S. P. Jiang, D. S. Silvester and T. Banerjee, *Ind. Eng. Chem. Res.*, 2022, **61**, 8763–8774.
52 X. Li, Z. Zhang, L. Yang, K. Tachibana and S.-I. Hirano, *J. Power Sources*, 2015, **293**, 831–834.
53 Z. Zhao, Y. Yin, X. Jin, G. Zhang, L.-M. Wang, Y. D. Liu and H. J. Choi, *ACS Appl. Nano Mater.*, 2021, **4**, 12382–12392.
54 R. Streck and A. J. Barnes, *Spectrochim. Acta, Part A*, 1999, **55**, 1049–1057.
55 T.-Y. Ma, L. Liu, Q.-F. Deng, X.-Z. Lin and Z.-Y. Yuan, *Chem. Commun.*, 2011, **47**, 6015–6017.
56 A. I. Bortun, L. Bortun, A. Clearfield, M. A. Villa-García, J. R. García and J. Rodríguez, *J. Mater. Res.*, 1996, **11**, 2490–2498.
57 Y. Brahmi, N. Katir, J. A. M. Agullo, A. Primo, M. Bousmina, J. P. Majoral, H. Garcia and A. El Kadib, *Dalton Trans.*, 2015, **44**, 15544–15556.
58 Y. Brahmi, N. Katir, A. Hameau, A. Essoumhi, E. M. Essassi, A.-M. Caminade, M. Bousmina, J.-P. Majoral and A. El Kadib, *Chem. Commun.*, 2011, **47**, 8626–8628.
59 M. Boundor, F. Semerci, N. Katir, S. Royer and A. El Kadib, *J. Energy Storage*, 2024, **79**, 110119.
60 Y. Brahmi, N. Katir, M. Ianchuk, V. Colliere, E. M. Essassi, A. Ouali, A.-M. Caminade, M. Bousmina, J. P. Majoral and A. El Kadib, *Nanoscale*, 2013, **5**, 2850–2856.
61 W. Ma, Z. Lu and M. Zhang, *Appl. Phys. A: Mater. Sci. Process.*, 1998, **66**, 621–627.
62 N. Katir, Y. Brahmi, J. P. Majoral, M. Bousmina and A. El Kadib, *Chem. Commun.*, 2015, **51**, 17716–17719.
63 Y. Zhou and M. Antonietti, *J. Am. Chem. Soc.*, 2003, **125**, 14960–14961.
64 J. Y. Lee, N. Y. Kim, D. Y. Shin, H.-Y. Park, S.-S. Lee, S. Joon Kwon, D.-H. Lim, K. W. Bong, J. G. Son and J. Y. Kim, *J. Nanopart. Res.*, 2017, **19**, 98.
65 L. Cen, K. Neoh and E.-T. Kang, *Adv. Mater.*, 2005, **17**, 1656–1661.
66 L. Azizova, D. Morgan, J. Rowlands, E. Brousseau, T. Kulik, B. Palianytsia, J. P. Mansell, J. Birchall, T. Wilkinson and A. Sloan, *Appl. Surf. Sci.*, 2022, **604**, 154462.
67 G. Mani, D. M. Johnson, D. Marton, V. L. Dougherty, M. D. Feldman, D. Patel, A. A. Ayon and C. M. Agrawal, *Langmuir*, 2008, **24**, 6774–6784.

68 J. Song, Z. Yu, M. L. Gordin, S. Hu, R. Yi, D. Tang, T. Walter, M. Regula, D. Choi and X. Li, *Nano Lett.*, 2014, **14**, 6329–6335.
69 X. Wu, K. Gong, G. Zhao, W. Lou, X. Wang and W. Liu, *RSC Adv.*, 2018, **8**, 4595–4603.
70 S. Wang, J. Lian, W. Zheng and Q. Jiang, *Appl. Surf. Sci.*, 2012, **263**, 260–265.
71 C. Rizzo, S. Marullo, P. R. Campodonico, I. Pibiri, N. T. Dintcheva, R. Noto, D. Millan and F. D'Anna, *ACS Sustainable Chem. Eng.*, 2018, **6**, 12453–12462.
72 S. Boudesocque, L. Viau, H. Nouali and L. Dupont, *Sep. Purif. Technol.*, 2023, **322**, 124285.
73 V. Amendola, R. Pilot, M. Frasconi, O. M. Maragò and M. A. Iatì, *J. Phys. Condens. Matter.*, 2017, **29**, 203002.
74 M. Boundor, B. Bielska, N. Katir, N. Wronska, K. Lisowska, M. Bryszewska, K. Miłowska and A. El Kadib, *ACS Appl. Polym. Mater.*, 2023, **5**, 9952–9963.
75 M. Boundor, N. Katir, S. Royer and A. El Kadib, *ACS Appl. Nano Mater.*, 2025, **8**, 639–648.